

Hexagonal pore geometry and the presence of hydroxyapatite enhance deposition of mineralized bone matrix on additively manufactured polylactic acid scaffolds

Anna Diez-Escudero^{a,b,*}, Brittmarie Andersson^a, Cecilia Persson^{b,1}, Nils P. Hailer^{a,1}

^a Ortholab, Department of Surgical Sciences—Orthopaedics, Uppsala University, Sweden

^b Biomaterial Systems, Department of Materials Science and Engineering, Uppsala University, Sweden

ARTICLE INFO

Keywords:

Additive manufacturing
Fused deposition modelling
Polylactic acid
Hydroxyapatite
Composites
Pore geometry
Osteogenesis
Mineralization

ABSTRACT

Additive manufacturing (AM) has revolutionized the design of regenerative scaffolds for orthopaedic applications, enabling customizable geometric designs and material compositions that mimic bone. However, the available evidence is contradictory with respect to which geometric designs and material compositions are optimal. There is a lack of studies that systematically compare different pore sizes and geometries in conjunction with the presence or absence of calcium phosphates. We therefore evaluated the physicochemical and biological properties of additively manufactured scaffolds based on polylactic acid (PLA) in combination with hydroxyapatite (HA). HA was either incorporated in the polymeric matrix or introduced as a coating, yielding 15 and 2% wt., respectively. Pore sizes of the scaffolds varied between 200 and 450 μm and were shaped either triangularly or hexagonally. All scaffolds supported the adhesion, proliferation and differentiation of both primary mouse osteoblasts and osteosarcoma cells up to four weeks, with only small differences in the production of alkaline phosphatase (ALP) between cells grown on different pore geometries and material compositions. However, mineralization of the PLA scaffolds was substantially enhanced in the presence of HA, either embedded in the PLA matrix or as a coating at the surface level, and by larger hexagonal pores. In conclusion, customized HA/PLA composite porous scaffolds intended for the repair of critical size bone defects were obtained by a cost-effective AM method. Our findings indicate that the analysis of osteoblast adhesion and differentiation on experimental scaffolds alone is inconclusive without the assessment of mineralization, and the effects of geometry and composition on bone matrix deposition must be carefully considered in order to understand the regenerative potential of experimental scaffolds.

1. Introduction

Despite the inherent regenerative potential of bone, larger defects require exogenous support that enhances or guides osteogenesis. Thus, autologous or homologous bone grafts are the most transplanted tissue after blood [1], but such resources are limited, and donor-site morbidity is a challenge subsequent to harvesting of autologous bone grafts [2,3].

Bone regenerative approaches focus on the development of optimal scaffolds that induce or sustain the process of bone healing, and their mechanical stability, physicochemical properties, and biological interactions with bone cells are of crucial importance. The emergence of additive manufacturing (AM) has enabled the development of new

designs and geometries intended for use as artificial bone scaffolds, and the combination of high-resolution imaging implemented in computer-aided design (CAD) and its translation into AM have demonstrated great potential [4–6]. For instance, fused deposition modelling (FDM) or fused filament fabrication (FFF) has been explored as low-cost technique to fabricate customized filament compositions and scaffold designs.

The combination of polymers with mineral phases, mainly calcium phosphates (CaP), is a common approach to engineer regenerative scaffolds [7–9]. The most common material used in FDM is polylactic acid (PLA), an aliphatic inexpensive biodegradable and biocompatible polyester that is already used in some commercially available medical devices such as meshes, suture anchors, screws and nails [10]. PLA

* Corresponding author at: Ortholab, Department of Surgical Sciences—Orthopaedics, Uppsala University, Sweden.

E-mail address: anna.diez@surgsci.uu.se (A. Diez-Escudero).

¹ Contributed equally.

possess important properties such as high tensile strength and modulus, and high elongation at breakage [11]. PLA production from non-fossil renewable resources, mainly starch-containing vegetables, further makes this polymer an excellent and eco-friendly candidate for use in biomedical applications [10]. Despite these excellent properties, the low toughness and limited bioactivity of PLA hamper its clinical applications. The incorporation of other polymers such as polycaprolactone (PCL) or polyurethane (TPU) confers improved mechanical performance [12–14], and polyethyleneglycol (PEG) has been explored as plasticizer and enhancer of surface wettability [15].

Some purely ceramic scaffolds based on hydroxyapatite (HA) confer good osteoconduction and osteoinduction with specific porous designs [16,17], but their use is limited to non load-bearing applications due to their inherent brittleness [18]. Mineral fillers have been used in conjunction with polymers to overcome the lack of bioactivity of pure PLA [19,20], and several studies have investigated the use of PLA- and CaP-customized filaments for use in FDM [8,21–23]. The combination of CaPs with polymers such as PCL has resulted in promising results [24], even with further magnetic features achieved through iron-doped nanoHA used in extrusion based techniques to obtain porous scaffolds which further enhanced cell viability [25]. On the other hand, CaPs combined with PLA have resulted in mild inflammatory responses [19,26], although, compared to tricalcium phosphates or demineralized bone matrix, HA seemed to improve *in vivo* resorption and yielded superior osteoinductivity [27]. Noteworthy, the use of a 3D-printed 15% HA-PLA porous composite in combination with autologous bone marrow stem cells in an *in vivo* bioreactor model demonstrated that the use of vascular bundles was pivotal in the reconstruction of large vascularized bone defects compared to periosteum implantation [28], highlighting the importance of vasculature around scaffolds for critical size defect repair. In addition, hitherto, PLA-based devices such as resorbable screws applied into clinics have performed unfavourably compared with conventional metallic screws [29,30]. Hence, it is of crucial importance to elucidate whether the addition of HA to 3D-printed PLA scaffolds can improve their mechanical and biological performance, rendering them suitable for use in critical size bone defects.

Apart from the composition of 3D-printed scaffolds, their overall porosity and the geometry and size of their pores are of paramount importance for bone regeneration. Macroporosity is known to affect the outcome of new bone tissue growth by allowing for cell migration and adhesion. The interconnectivity of pores is crucial by enabling nutrient supply to the cells colonizing the scaffolds [31]. Despite the heterogeneity between studies, pore sizes between 100 and 500 μm are commonly believed to enhance the osteoconductivity of porous scaffolds, and submicron- and nanoporosities are important for protein attachment [32]. The shape of pores is also important, with micro-concavities or sharp-angled pores being beneficial for angiogenesis and osteogenic differentiation [33]. In addition, certain pore geometries confer improved mechanical stability of composite scaffolds, with an increase in compressive strength associated with the incorporation of HA combined with hexagonal pores [34].

Given the vast number of studies and disparity of methodologies, the potential synergy of composition and porosity is difficult to elucidate. Studies with polymers such as PLA or PCL, with or without mineral fillers are contradictory. Nyberg et al. reported higher mineralization using adipose derived stem cells on 500 μm porous 3D printed scaffolds when decellularized bone was used rather than when HA was present [35], pointing at biological improvement from natural ceramics compared to synthetic ones. Other porous conformations obtained through lyophilisation using PLA and HA showed better mesenchymal stem cell spreading and proliferation when the HA size was in the nanoscale range compared to microscale particles or pristine PLA [36]. Danoux et al. found that PLA in combination with HA induced greater heterotopic bone formation after 12 weeks than pure PLA, although the degradation of composite PLA/HA was hampered [19]. Similarly,

Yaganida et al. found greater cell colonization on HA-coated PLA fabric than on non-coated PLA [37].

Taking into account the numerous variables affecting osteoconductivity, it is difficult to draw firm conclusions on the optimal composition and porosity of composite scaffolds intended for the repair of critical size bone defects. Despite the large variations in designs for 3D printed scaffolds, there is less variability in the composite composition with regard to the amount of HA incorporated. This is often related to the printing technique, as the mineral filler amount can impact printing fidelity. For instance, high amounts of mineral may result in reduced printability or nozzle clogging for the FDM technique. The most common ranges used for HA-PLA composites in FDM vary between 5 and 15% wt. [6,23,26–28,38,39], although few studies have successfully incorporated larger amounts such as 25 [8], 30 [23,40] and 50% wt. [8,22], either by using twin-screw extruders or by reducing the particle size of the filler to the nanometric range and controlling the dispersion within the polymeric matrix. Given the paucity of investigations comparing the presence or absence of HA in 3D-printed PLA scaffolds with systematic variations in pore size and geometry we set out to compare nine different substrates: One group of scaffolds consisted of pure PLA, one of a PLA/HA composite with a nominal filler amount of 15% HA based on previous literature, and finally one group of HA-coated PLA. The HA coating was aimed at elucidating possible effects of HA being directly exposed to cells as opposed to HA being embedded in the polymer, as in the composite PLA/HA. In addition to varying their composition, we manufactured and investigated non-porous scaffolds and scaffolds with either triangular or hexagonal pores of different sizes based on previous literature demonstrating the osteogenic potential of concavities and acute and obtuse angles. We then compared the physicochemical and biological properties of these substrates.

2. Materials and methods

2.1. Materials

2.1.1. Filament preparation

Two filaments were used for 3D printing, as received pristine PLA (3D4Makers.com, Waarderweg, Haarlem, Netherlands) with a thickness of 2.85 mm, and PLA with 15% wt. HA, so-called PLA15HA. The composite PLA15HA filament was prepared by solvent mixing with dichloromethane (Merck KGaA, Darmstadt, Germany). HA powders (Merck KGaA, Darmstadt, Germany) were sieved below 75 μm , weighted and placed in 500 mL of dichloromethane for 1 h to homogeneously disperse them under agitation. PLA filament was cut into pellets using a shredder (SHR3D IT, 3DEVO, Netherlands), weighted and placed onto the same HA dispersion, and left for dissolution and homogenization for approximately 3 h. Afterwards, the mixture was poured into a crystallizer and left for solvent evaporation. The film obtained was cut and further grinded into small flakes with a shredder (SHR3D IT, 3DEVO, Netherlands). The flakes were fed into a single screw extruder (Precision 350, 3DEVO, Netherlands), and extruded with a temperature gradient along the screw from 170 to 180 $^{\circ}\text{C}$, a screw speed of 5 rpm, and a fan speed of 70%, producing a filament with an average thickness of 2.85 mm.

2.1.2. Sample modelling

Fused deposition modelling (FDM) was used as 3D printing technique to obtain the different scaffolds. An Ultimaker S5 (3D Verktan AB, Stockholm, Sweden) was used to 3D print the structures, after using Cura Ultimaker software for slicing the generated structures. Scaffolds with 10 mm in diameter and 3 mm height were produced with different pore geometries. Triangles and hexagons were the controlled mono-disperse pore geometries studied. The porous scaffolds were obtained by slicing the 10 mm diameter and 3 mm height designs with different infill parameters through Cura software. Pristine PLA scaffolds were printed with a layer height of 60 μm , and a line width of 200 μm using a brass

nozzle of 0.4 mm; dense scaffolds were obtained by 100% infill printing with line pattern, triangle PLA were obtained with a triangular pattern with an infill distance of 1 mm, without top and bottom walls, and hexagons, similarly, by using a hexagonal pattern with an infill distance of 1 mm. Composite PLA-15HA scaffolds were produced similarly using a ruby nozzle of 0.6 mm diameter instead, with the same layer height as pristine PLA, and a line width of 500 μm , while keeping the same infill pattern and infill distance.

2.1.3. Sample preparation

Three types of substrates with three different types of infill were 3D printed. The different substrates consisted of pristine PLA, composite PLA15HA, and HA-coated PLA (PLACHA). Each substrate was printed with dense, triangular or hexagonal geometries. PLA and composite PLA15HA were used as printed. The HA-coated PLA (PLACHA) was prepared by etching the PLA scaffolds in ammonia, followed by HA coating in ethanol, as described elsewhere [37]. Briefly, PLA printed scaffolds were immersed in ammonia solution (28–30% NH_3 basis, Merck KGaA, Darmstadt, Germany) for 1 h under agitation at room temperature. Afterwards, scaffolds were rinsed and dried in air. The coating was carried out using a suspension containing the 1% wt. HA in absolute ethanol. The etched scaffolds were immersed in the HA suspension overnight under agitation at room temperature. Finally, the scaffolds were rinsed with ethanol, sonicated for 5 min, and dried in air.

2.2. Sample characterization

2.2.1. Thermal properties

Differential scanning calorimetry (DSC, DSC3, Mettler Toledo, Greifensee, Switzerland) and thermogravimetric analyses (TGA, Q500 V20, TA instruments, Newcastle, DE, USA) were performed for each substrate in triplicate. A heat/cool/heat method from room temperature to 190 $^{\circ}\text{C}$ at 10 K/min, cooling to -40°C at 5 K/min, and again to 190 $^{\circ}\text{C}$ under 50 mL/min nitrogen flow rate was used for DSC measurements. The glass transition temperature was obtained from the inflection point in the DSC thermograms, and the degree of crystallinity was measured by the enthalpies corresponding to melting and cold crystallization transitions, according to Eq. (1). Data are expressed as mean and standard deviation from three independent measurements.

$$X_c = \frac{\Delta H_m - \Delta H_C}{\Delta H_m^0 \left(1 - \frac{\% \text{weight filler}}{100}\right)} \quad (1)$$

where ΔH_m corresponds to the melting enthalpy, ΔH_C is the cold crystallization enthalpy, and ΔH_m^0 is the enthalpy of 100% crystalline PLA, corresponding to 93.7 J/g [41].

TGA was performed on each substrate from room temperature up to 600 $^{\circ}\text{C}$ under nitrogen flow of 50 mL/min and a heating rate of 10 $^{\circ}\text{C}/\text{min}$. The degradation temperature was obtained by the first derivative from the TGA curves.

2.2.2. Physicochemical properties

X-ray diffraction (XRD, D8 Advance, Bruker, Germany) was used to characterize phase composition using a $\text{Cu K}\alpha$ anode from 10 to 60 $^{\circ}$, and compared to standards from HA and DCPA (JCDPS 01-074-0565 and 04-009-3755, respectively). DIFFRAC.EVA software was used for semi-quantitative quantification of the phases in the HA powders. Attenuated total reflectance Fourier transform infrared spectroscopy (ATR-FTIR, Tensor 27, Bruker, Germany) equipped with a KBr beam splitter and a RT-DLaTGS detector was used to investigate the chemical characteristics of the scaffolds. Spectra were acquired using 1024 scans with a resolution of 4 cm^{-1} in the range of 4000–400 cm^{-1} with a diamond crystal.

Topological and morphological characteristics of the PLA-based scaffolds were investigated by scanning electron microscopy (SEM,

Merlin Zeiss, Germany). The scaffolds were observed as printed after a thin gold-palladium sputtering yielding a 5 nm coating. Image analysis through ImageJ® was used to analyse pore sizes using an average of 30 to 40 pores. The surface chemistry was further investigated by energy dispersive X-ray (EDX-SEM, Merlin Zeiss, Germany). Surface properties were analysed by white light interferometry (WLI, NexView Zygo, Ametek Inc., Germany) using a scanned area of $6 \times 6 \text{ mm}^2$. The surface roughness was measured at six different positions for each sample, and three samples were analysed per material substrate and geometry.

2.2.3. Biological characterization

The biological activity of the PLA-based scaffolds was investigated using two different cell types. Firstly, a pre-osteoblastic osteosarcoma cell line (SaOs-2, ECACC Sigma Aldrich, United Kingdom) was used. Prior to seeding, the scaffolds were placed in 24 well plates and disinfected by immersion for 3 h in 70% ethanol, followed by three rinses of phosphate-buffered saline (PBS, Gibco, Merck, KGaA, Darmstadt, Germany). Finally, 1 mL of complete media consisting of Dulbecco's modified Eagle's medium low glucose (DMEM, Merck, KGaA, Darmstadt, Germany), 10% fetal bovine serum (FBS, Merck, KGaA, Darmstadt, Germany) and 1% penicillin/streptomycin (Merck, KGaA, Darmstadt, Germany) was added and left overnight for protein adhesion. A droplet method with high viscosity modified media adapted from the literature was used for seeding [42]. Modified viscous media were prepared with DMEM, 25% FBS, and 2.5% penicillin/streptomycin, and diluted in 60% vol. Ficol-Paque™ Plus (GE Healthcare, Uppsala, Sweden) and used as seeding media, yielding a final concentration of 60% Ficol, 10% FBS, and 1% antibiotic. A droplet of 50 μL of modified viscous media containing $2 \cdot 10^6$ cells was seeded on top of the scaffolds, giving a final concentration of 10^5 cells/mL. After seeding, the scaffolds were placed in the incubator for 3 h for cell attachment. After this time, 950 μL of complete media was added to each well. Samples consisting of glass cover slips (12 mm diameter) were used as controls. Complete media was added to control samples immediately after the droplet seeding to avoid drying in the incubator.

Secondly, mouse osteoblasts (mOB) primary cells were used on the same scaffolds, and seeded similarly, with the only variation of a final concentration of $5 \cdot 10^4$ cells/mL, and cell media based on high glucose DMEM (DMEM high glucose, Merck, KGaA, Darmstadt, Germany). All animal experiments were approved by the Uppsala Ethical Committee on Animal Welfare (150,130, approval numbers C1/15). Mouse osteoblasts (mOB) were isolated from femoral and tibial diaphyses of 9–10 week mice. Briefly, bones were cut into 1–2 mm dices, placed into Falcon tubes and incubated in 2 mg/mL collagenase (Merk, KGaA, Darmstadt, Germany) solution in DMEM high glucose for 2 h. Afterwards bone dices were rinsed with media (DMEM high glucose) containing 10%FBS, and 1% penicillin/streptomycin three times, and transferred to 25 cm^2 flasks for expansion. Cells passaged 3 to 5 were used for all experiments. Three biological replicas with three technical replicas for each type of scaffold were used for SaOS-2 and mOB experiments. Controls consisting of tissue culture polystyrene (TCPS) were included in all experiments.

In order to compare the cellular yield of SaOs-2 and mOB with different cell densities, an adhesion test with $5 \cdot 10^4$ cells/mL of each cell type was performed on hexagonal pore scaffolds as the most conservative adhesion substrate (supplementary material), showing similar yields.

Cell cultures were sustained for up to 28 days, and analysed after one, 14, and 28 days. Media were exchanged every two days, and after one week of cell culture, normal media were replaced by osteoinductive media where 10 mM beta-glycerophosphate, 100 nM dexamethasone, and 80 μM ascorbic acid (all purchased from Merck, KGaA, Darmstadt, Germany) were added to the basal media used for each cell type.

Fluorescent imaging was performed on the scaffolds with either cell type after 28 days and observed using a Leica microscope (Leica Dmi8, Microsystem CMS GmbH, Wetzlar, Germany). Cells were fixed using 4% (v/v) paraformaldehyde for 15 min at room temperature, followed by

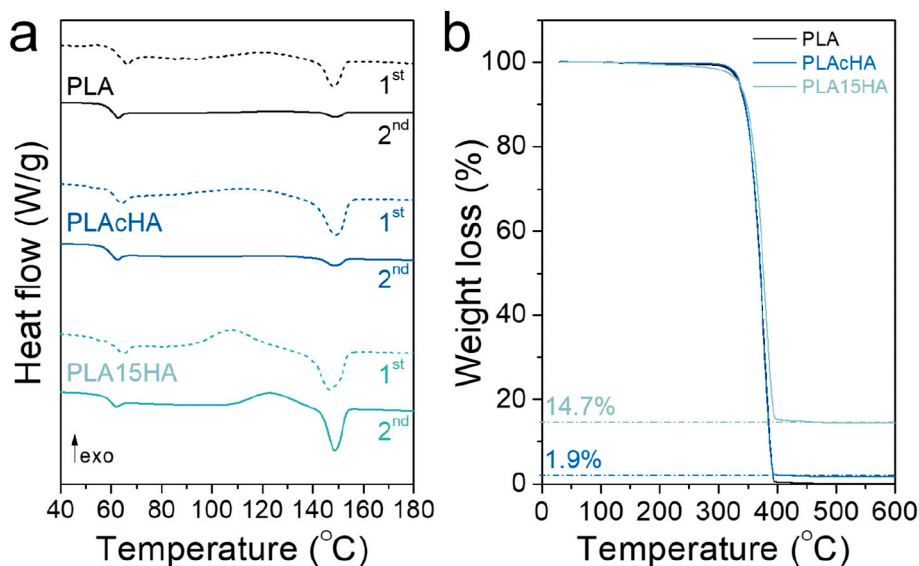


Fig. 1. DSC representative thermograms (a) for first and second heating (dashed and solid line, respectively), and thermogravimetric analyses (TGA) for the three different substrate types used, pristine PLA, hydroxyapatite coated HA (PLAcHA) and 15% wt. HA composite PLA (PLA15HA).

three rinses with PBS and membrane permeabilization with 0.1% Triton X-100 (Merk, KGaA, Darmstadt, Germany) in PBS for 20 min at room temperature. Afterwards, scaffolds were rinsed thrice with PBS and cell cytosol was stained with carboxyfluorescein diacetate (500 nM, 400 μ L CFDA, Merck, KGaA, Darmstadt, Germany) for 15 min at room temperature in the dark, and cell nuclei were stained using 4',6-diamidino-2-phenylindole (300 nM, 400 μ L DAPI, Invitrogen, Massachusetts, USA) for 1 h at room temperature in the dark. Finally, scaffolds were rinsed thrice with PBS and observed under the microscope.

Cell viability and proliferation was assessed on cell lysates at each time point by lactate dehydrogenase enzymatic assay (LDH, Tox7, Merck, KGaA, Darmstadt, Germany) according to manufacturer and absorbance was measured in a spectrophotometer at 690–490 nm (Multiscan Ascent, Thermo Fisher Scientific Inc., Waltham, MA). Cell differentiation was evaluated through alkaline phosphatase (ALP, Merck, KGaA, Darmstadt, Germany) measured at 405 nm, and normalized by the total protein in cell lysates measured by BCA (Pierce™ Coomassie Bradford Protein Assay Kit, Thermo Fisher Scientific Inc., Waltham, MA) at 540 nm.

Cell mineralization in experiments on mOB was studied through alizarin red (AR) staining and quantification after 14 and 28 days. At each time point, cells on scaffolds were fixed using ice cold 70% ethanol for 1 h at room temperature. Then, the scaffolds were rinsed with distilled water and stained using alizarin red staining (40 mM AR solution, Merck, KGaA, Darmstadt, Germany) at pH 4.2 for 10 min at room temperature. Afterwards, stained scaffolds were rinsed with distilled water several times, and followed by a final rinse in PBS for 15 min in a shaker to remove unspecific AR staining. To quantify AR staining, the scaffolds were decolorized using 10% wt. cetylpyridinium chloride (CPC, Merck, KGaA, Darmstadt, Germany) in 10 mM sodium phosphate solution for 20 min in a shaker at room temperature, and the supernatants were collected and measured in a spectrophotometer at 562 nm. Control samples consisting of the same printed scaffolds, and cultured with media in the same conditions but without cells were used and treated similarly. The absorbance readout for control samples was subtracted from each respective sample as background. Additionally, glass cover slips were used as internal controls. Three biological replicas with two technical replicas were used for mineralization quantification.

Table 1

Thermal properties of the 3D printed substrates obtained from DSC and TGA quantitative analysis; DSC values calculated from the second heating curves are expressed as mean and standard deviation from three independent measurements; X_c refers to the crystallinity degree obtained from the second heating endotherm from DSC and Eq. (1).

	T _g (°C)	T _{cc} (°C)	T _m (°C)			T _{deg} (°C)	X _c (%)
			T _{onset}	T _{peak}	T _{endset}		
PLA	58 ±	–	143 ±	149 ±	154 ±	379	2.2 ±
	0.3		0.2	0.4	0.4		0.5
PLAcHA	58 ±	–	143 ±	149 ±	153 ±	380	2.9 ±
	0.2		0.3	0.3	0.1		0.2
PLA15HA	58 ±	123 ±	143 ±	149 ±	153 ±	381	5 ± 1
	0.2	0.2	0.1	0.3	0.2		

2.3. Statistical analyses

Pore size values are presented using mean \pm standard deviation. Data derived on cell studies are described using means \pm standard errors. Levene's test was used to ascertain homogeneity of variance, and differences between group means were assessed by one-way ANOVA and Tukey's post-hoc test. The threshold of statistical significance was set at $p < 0.05$.

3. Results

3.1. Thermal characterization

The thermal characterization of the three different scaffold compositions is depicted in Fig. 1a, exhibiting both the first (dotted line) and the second heating (solid line) obtained from the DSC measurements, and the degradation temperature and filler amount from TGA (Fig. 1b). In general, larger variations were observed for the composite PLA15HA samples in terms of crystallinity compared to pristine PLA and HA-coated PLAcHA. The glass transition temperature (T_g) and the melting temperature (T_m) for PLA and PLAcHA samples showed similar values, around 59 °C, and 149 °C, respectively (Table 1), with a decrease in T_g for composite PLA15HA samples. A recrystallization phenomenon (T_{cc}) was observed for the composite PLA15HA (Fig. 1a) and reflected in the crystallinity degree. This phenomenon was only observed in the first

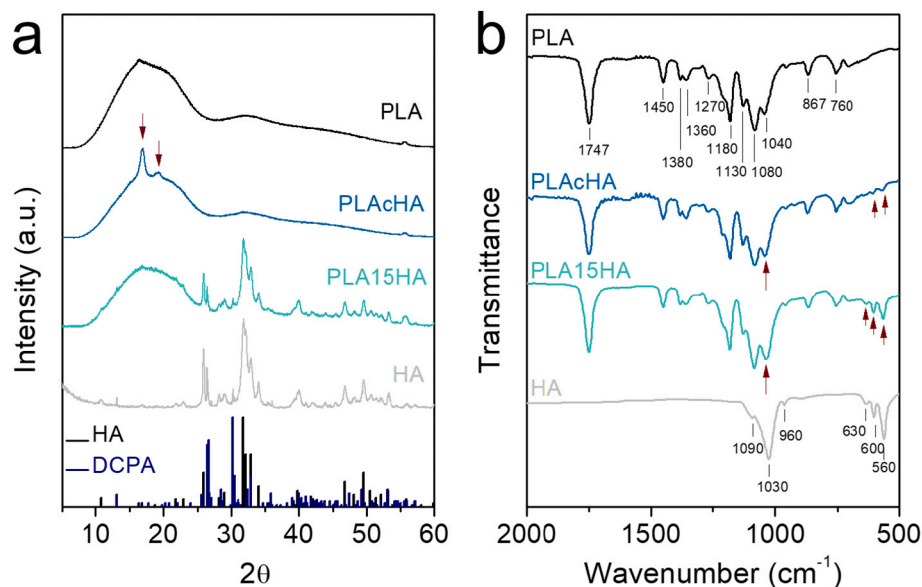


Fig. 2. (a) Phase composition of the three different substrates analysed by XRD, corresponding to pristine PLA, HA-coated PLA (PLAcHA) and composite PLA15HA; HA powders used for compounding and coating are depicted in grey. (b) ATR-FTIR spectra of the substrates. (For interpretation of the references to color in this figure, the reader is referred to the web version of this article.)

heating endotherm of PLA and PLAcHA samples. All substrates showed an enthalpy relaxation phenomenon near their T_g , which was reduced in the second heating endotherm (Fig. 1b). The degradation temperatures were similar for all substrates, with a slight increase for the composite PLA15HA.

TGA analyses exhibited a reduction of the onset degradation temperature for the composite PLA15HA sample compared to pristine and coated PLA; all substrates exhibited similar degradation temperatures, with PLA15HA depicting a slight increase of less than 2 °C. The incorporation of HA mineral was confirmed for the composite PLA15HA, with a final yield of 14.7% wt., while the HA coating showed a total HA incorporation of approximately 2% wt. (Fig. 1b).

3.2. Physicochemical characterization

The phase composition analysed through XRD (Fig. 2a) for each type of substrate showed the amorphous nature of PLA. On the other hand, the HA powder used for both the composite and the coated PLA resulted in typical peaks, corresponding to HA and dicalcium phosphate anhydrous (DCPA)/monetite (JCPDS 09-0432 for HA and 09-0080 for DCPA), accounting for 91.1% and 8.9% wt., respectively. The composite PLA15HA scaffolds depicted the incorporation of HA into the amorphous PLA, showing the same peaks as HA pristine powders. The HA-coated scaffolds, on the contrary, depicted a similar composition as the pristine PLA, with the appearance of small peaks at 16.4° and 19° (Fig. 2a, black arrows) compatible with the formation of lactides due to the etching process [7,43]. No peaks corresponding to HA were detected

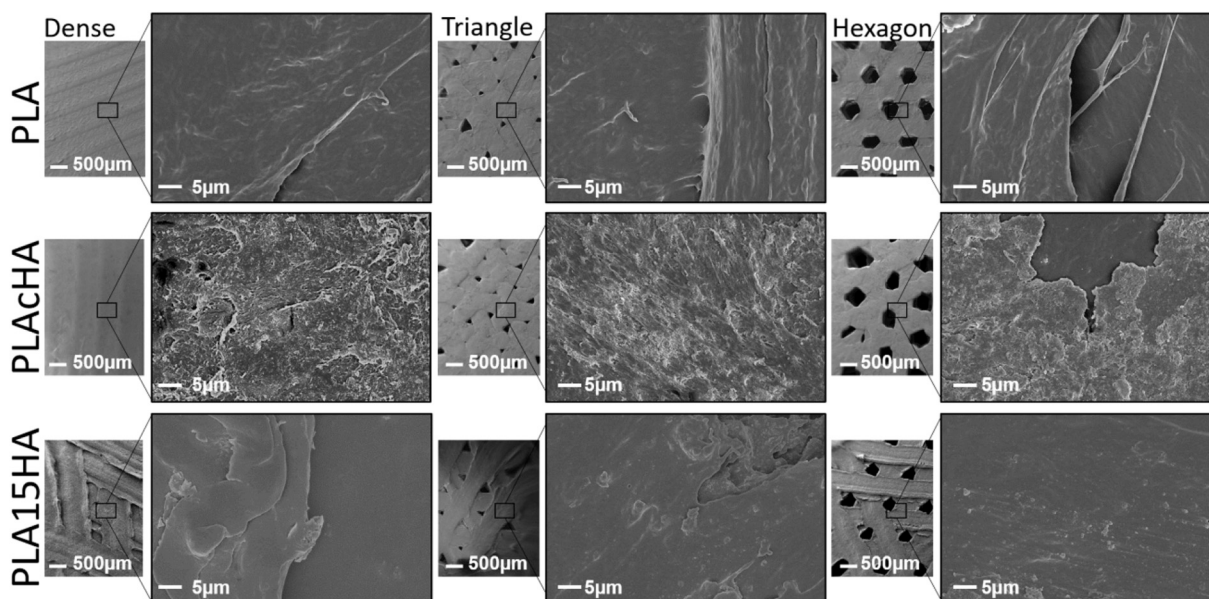


Fig. 3. SEM images of the top-view from all different scaffolds' substrate and geometry. First row depicting dense, triangle and hexagon geometries for pristine PLA; second row for HA-coated PLA (dense, triangle, and hexagon, from left to right); and third row showing composite PLA15HA.

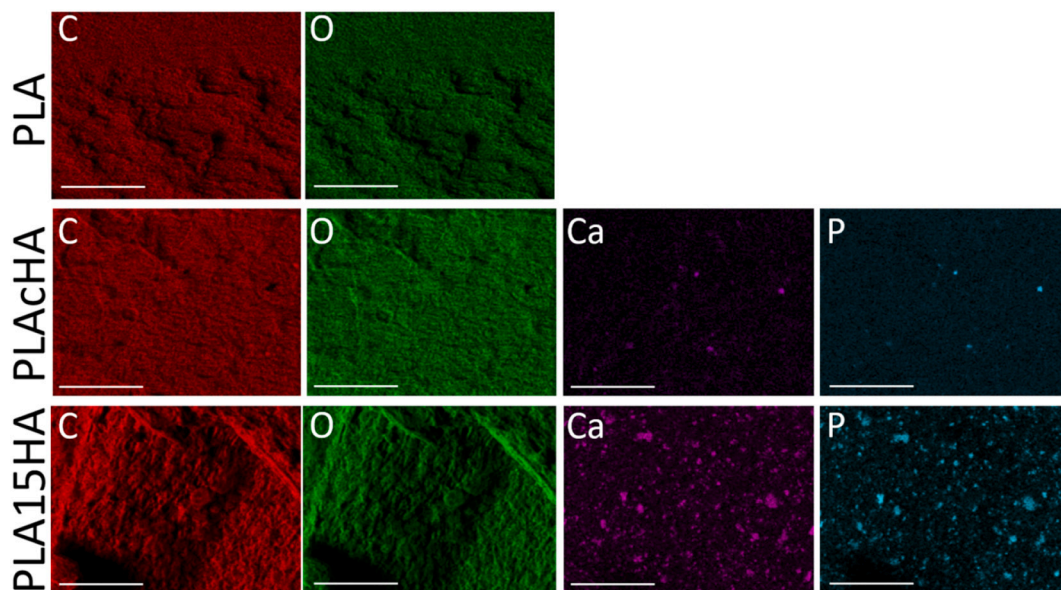


Fig. 4. EDX colour mapping for PLA (first row) showing the signal for carbon and oxygen (C-red, O-green, respectively); HA-coated PLA (second row) depicting the presence of C, O and calcium (Ca-pink) and phosphorus (P-blue); and composite PLA15HA (third row) depicting same elements, C, O, Ca and P; (scale bar: 100 μm). (For interpretation of the references to colour in this figure legend, the reader is referred to the web version of this article.)

for the PLACHA samples.

The ATR spectra for HA (Fig. 2b) showed typical bands at 560, 600, and 960 cm^{-1} , 1030 and 1030 cm^{-1} corresponding to ν_4 , ν_1 and ν_3 of phosphate (PO_4^{3-}). Hydroxyl band for the HA powders was observed at 630 cm^{-1} . The pristine PLA exhibited bands at 1747 cm^{-1} corresponding to carbonyl groups, 1450 cm^{-1} corresponding to methyl groups,

1380 and 1360 cm^{-1} for CH-CH_3 , 1270 cm^{-1} corresponding to CH-C-O , and 1180 and 1080 cm^{-1} from ester groups C-O-C . Bands at 1040 cm^{-1} corresponded to C-CH_3 , and bands at 867 and 760 cm^{-1} were ascribed to carbonyl group C=O . The composite PLA15HA depicted increased intensity from the bands corresponding to phosphate groups (Fig. 2b, red arrows). ATR spectra depicted the presence of HA in

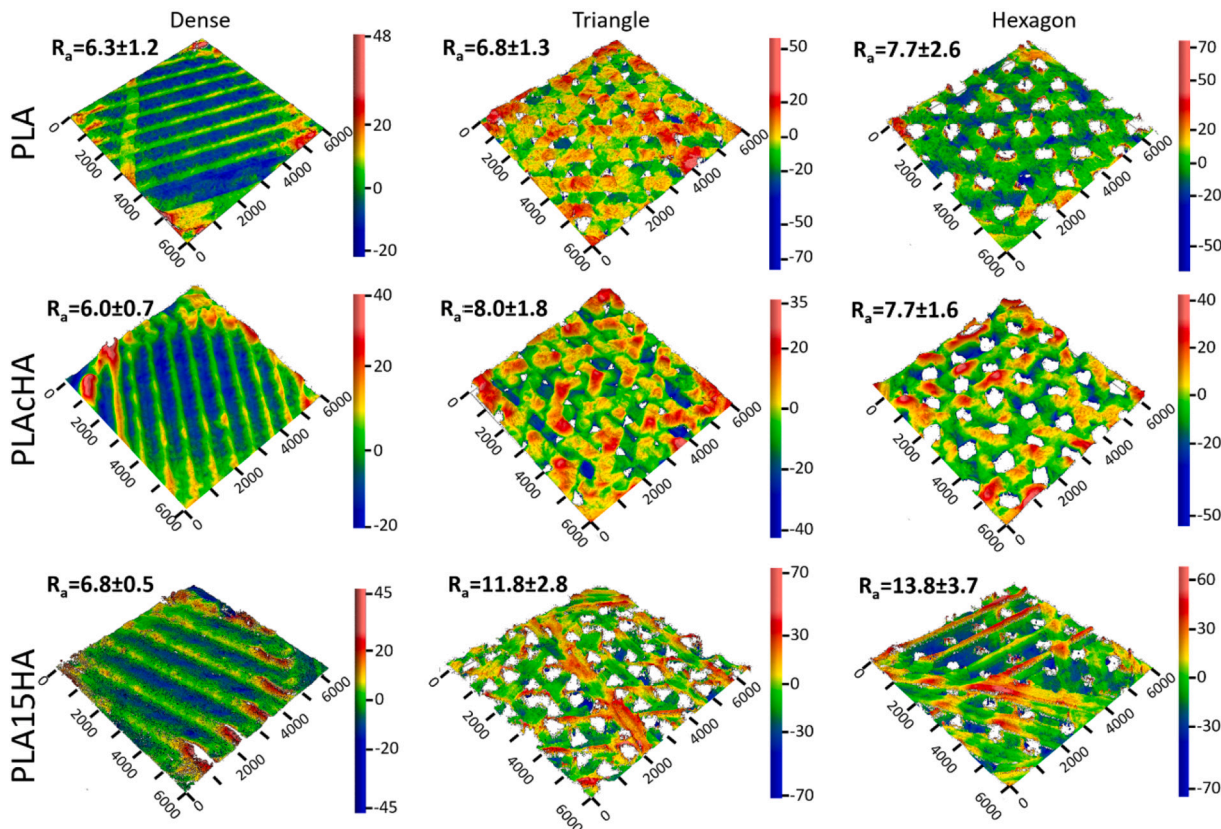


Fig. 5. WLI analyses showing the average surface roughness for each substrate and geometry (scanned area $6 \times 6 \text{mm}^2$); first row corresponding to pristine PLA, second row for HA-coated PLA, and third row for composite PLA15HA (from left to right columns: dense, triangle, and hexagon geometries).

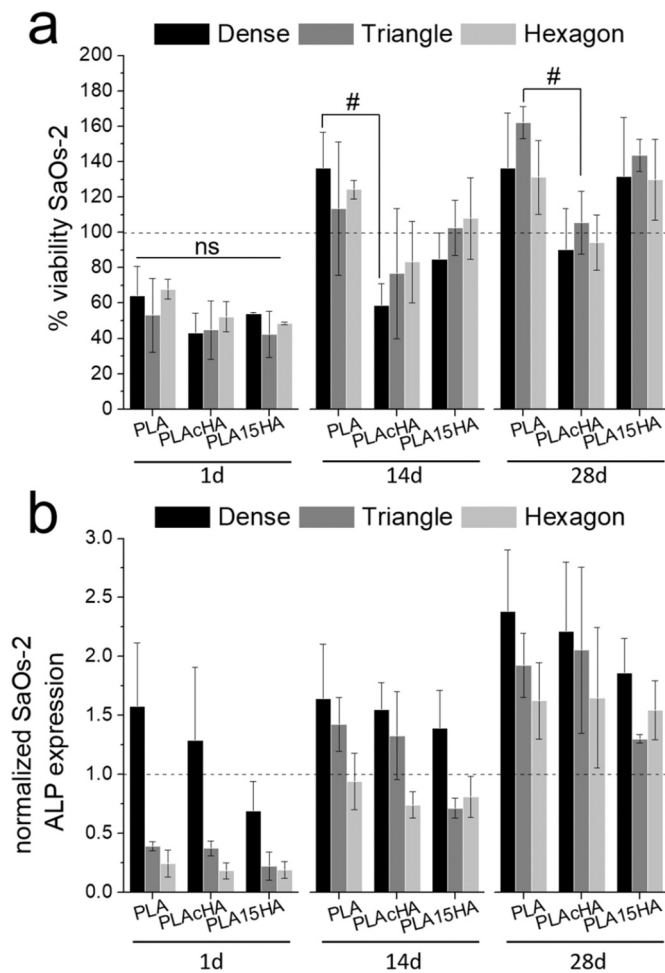


Fig. 6. SaOs-2 cell cultures on the different substrates and geometry; D, T, and H subscripts referring to dense, triangles, and hexagons, respectively, and substrates referred as PLA for pristine PLA, PLACHA for HA-coated PLA, and PLA15HA for the composite PLA with 15% wt. HA. (a) Cell proliferation over time measured by LDH and normalized to the area of the scaffolds and expressed as % compared to control samples (TCPS) at each time point (dotted line signifies 100% corresponding to controls); (b) ALP expression normalized to control samples (glass coverslips); # denotes statistical significance between the different type of substrates for each geometry ($p < 0.05$), ns stands for not significant ($p \geq 0.05$).

PLACHA samples by the increase in the band corresponding to phosphates at 560, and 600 cm^{-1} (Fig. 2b red arrows), together with an increase at 1040 cm^{-1} , relatively higher compared to 1080 band for pristine PLA (Fig. 2b red arrows).

SEM was used to investigate the surface topography of the different substrates (Fig. 3). Pristine PLA scaffolds exhibited a smooth surface regardless of the scaffold geometry. The presence of the extrusion struts from the printing procedure was noticeable, with some threads at the interface between layers. Oppositely, the HA-coated PLA (PLACHA) scaffolds clearly depicted the presence of a rough mineral coverage. The composite substrates consisting of PLA15HA also had a rougher surface compared to pristine PLA, with noticeable crystals embedded in the polymer matrix.

Image analyses performed on the SEM images acquired for porous scaffolds quantified the pore sizes for triangular pore geometry as $190 \pm 50 \mu\text{m}$ for PLA, $200 \pm 60 \mu\text{m}$ for PLACHA, and $190 \pm 20 \mu\text{m}$ for PLA15HA. Hexagonal geometries exhibited larger pores, with values of $500 \pm 80 \mu\text{m}$ for PLA, $500 \pm 90 \mu\text{m}$ for PLACHA, and $400 \pm 35 \mu\text{m}$ for the composite PLA15HA.

The incorporation of HA mineral in the structure of both coated and

composite PLA was evidenced by EDX (Fig. 4). Pristine PLA contained only carbon and oxygen, as commonly encountered in polymers; however, HA-coated PLA (PLACHA) exhibited few particles consisting of calcium and phosphorus derived from the HA. The incorporation of HA was evident in composite PLA (PLA15HA), with more intense signals from both calcium and phosphorus, resulting in a homogeneous distribution.

Surface roughness measured through interferometry further evidenced the differences in topography between the three different substrates and the influence of their respective geometries (Fig. 5). The incorporation of HA in the PLA matrix for PLA15HA depicted the highest roughness, followed by coated PLACHA and pure PLA analogues, regardless the geometry type. With regards to geometry, dense samples showed the smoother surfaces, as expected from the absence of pores. The highest roughness values were found for triangular and hexagonal geometries for all scaffolds, with a pronounced increase for the composite scaffolds, yielding 12 μm and 14 μm for triangular and hexagonal pore scaffolds, respectively.

3.3. Biological characterization

Cell proliferation studies using SaOs-2 cells indicated lower viability on all scaffolds at 1 day compared to control samples consisting of glass coverslips, without statistically significant differences between different geometries or compositions (Fig. 6a). After 14 days of culture, cell viability for SaOs-2 cells was higher on pristine PLA substrates, followed by composite PLA15HA, and HA-coated PLACHA being the least efficient substrate in terms proliferation, regardless of the geometry type. In terms of geometry, lowest proliferation was found on dense HA containing scaffolds, higher on triangular pore scaffolds, and highest on hexagonal ones, although no statistical significance was found. The only statistically significant difference was found for dense pristine PLA scaffolds with higher viability compared to HA-coated PLACHA. After 28 days of cell culture, cell proliferation was similar on pristine PLA and composite PLA15HA scaffolds irrespective of pore geometry, while the lowest viability was found on HA-coated PLACHA. Triangular pore geometries gave rise to the highest viabilities on all substrates, but without statistical significance.

ALP expression of SaOs-2 cells was higher on both PLA and HA-coated PLACHA dense scaffolds at 1 day (Fig. 6b). After 14 days and 28 days of culture, the highest ALP expression was observed for PLA scaffolds, followed by PLACHA, and PLA15HA. All substrates stimulated ALP expression more than control samples. With regards to the type of geometry, dense scaffolds induced the highest ALP values, followed by those with triangular pores, and lowest for hexagonal pore scaffolds.

SaOs-2 cell fluorescence imaging at the end of the cell culture (28d) illustrated coverage of all scaffold surfaces, depicting cell aggregation especially on HA-coated PLACHA with triangular pores and on composite PLA15HA with hexagonal pores (Fig. 7). Cell aggregation was enhanced inside the edges of hexagonal pores in composite PLA15HA, showing several layers of cell accumulation along the pore depth.

Results of culturing mouse primary osteoblasts (mOB) on scaffolds are illustrated in Fig. 8. No statistically significant differences in cell viability between the different compositions were observed after 1 day. After 14 days of culture, a decrease in proliferation compared to control was observed, although an increment was found after 28 days compared to the previous time point. The viability after 1 day was lower on HA-containing scaffolds, similarly to 14 days; however, after 28 days, cell viability was higher on HA-coated PLACHA, and similar for PLA and PLA15HA. Highest viability was observed for mOB grown on triangular pore scaffolds at 14 and 28 days, followed by dense geometries, and the lowest values observed for PLA15HA.

The ALP expression of mOB was highest on HA-coated PLACHA after 1 and 14 days, followed by composite PLA15HA, and pristine PLA inducing the lowest ALP values. Overall, the lowest values of ALP were observed on hexagonal pore scaffolds, followed by triangular ones,

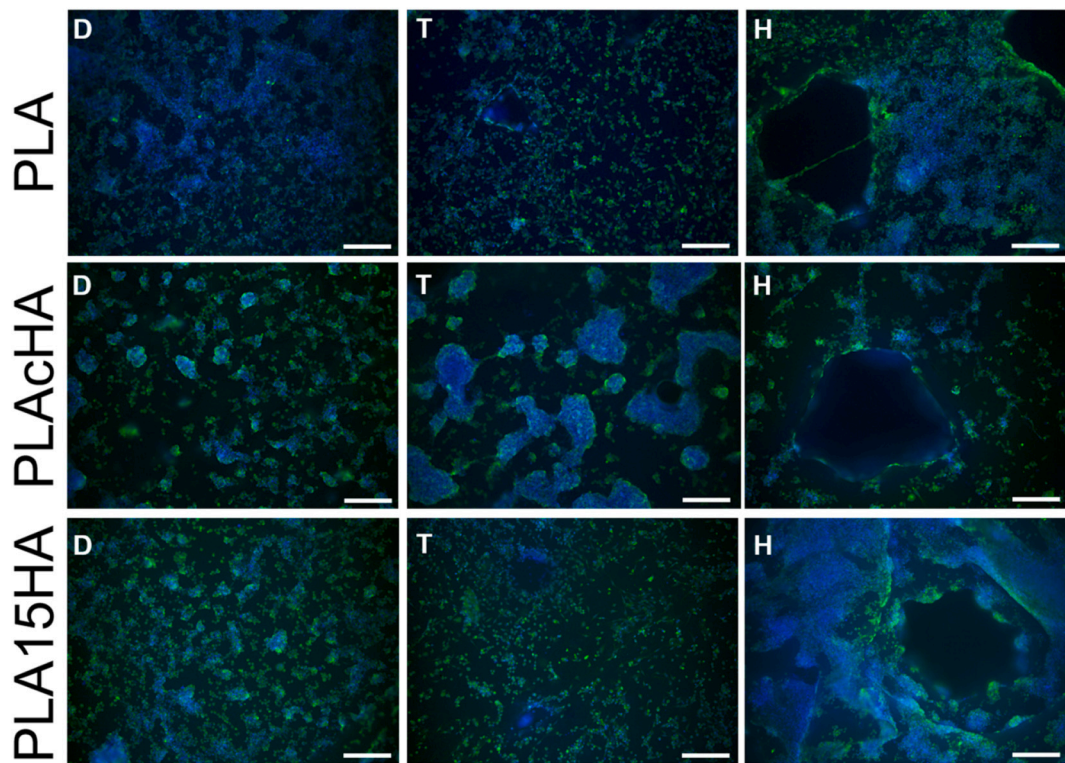


Fig. 7. Fluorescence images of the three substrates and geometries cultured with SaOs-2 after 28 days; D, T, and H correspond to dense, triangle and hexagon, respectively. First row and column insert shows a higher magnification image of dense PLA substrate cell alignment along the 3D printed threads (DAPI: blue, CFDA: green, scale bar: 200 μm). (For interpretation of the references to colour in this figure legend, the reader is referred to the web version of this article.)

whereas mOB grown on dense scaffolds had the highest ALP values at all-time points, except for triangular pore PLAcHA scaffolds after 14 days and 28 days, although not statistically significant.

Fluorescence imaging of mOB after 28 days of culture showed cells covering the surfaces of all scaffolds (Fig. 9). Pristine PLA scaffolds with a dense geometry had areas of cells aligned along the threads of the deposited material during the 3D printing process (Fig. 9 insert). HA-coated PLAcHA exhibited cell matrix bridging triangular and hexagonal pore scaffolds. The matrix bridging was observed in all scaffolds with hexagonal pores. Bright field images were acquired for porous scaffolds, and the mentioned matrix deposition was observed inside the edges and concavities (black arrows) of both triangular and hexagonal pores, although no deposition was found on the pristine PLA scaffolds.

The mineral deposition of primary mOB on the different substrates was investigated by AR staining. Visual inspection after 28 days indicated that mineral deposition was highest on PLA15HA scaffolds, followed by PLAcHA scaffolds, and lowest on pristine PLA scaffolds (Fig. 10a). AR quantification indicated increased mineralization in the presence of HA; mineralization after 14 days was highest on composite PLA15HA scaffolds, followed by HA-coated PLAcHA, while pure PLA scaffolds exhibited the lowest AR values (Fig. 10b). When comparing pore geometries, mineralization was higher on scaffolds with hexagonal or triangular pores than on dense. After 28 days, an increased upregulation of mineralization was observed on composite PLA15HA scaffolds, followed by HA-coated PLAcHA scaffolds. The lowest AR values were found on pristine PLA scaffolds, regardless whether pores were present or not. Overall, the highest mineralization was consistently observed on hexagonal pore scaffolds, especially in the presence of HA.

4. Discussion

Recent developments in AM have motivated a plethora of studies focused on the production of customizable designs and material

combinations intended for bone regenerative scaffolds [44,45]. FDM stands as one of the most inexpensive 3D printing techniques, which allows for production of a variety of porous structures, highly reproducible and with overall good mechanical properties [44]. Although the printing resolution of complex designs is more limited than with other printing techniques and the incorporation of biological factors cannot take place in situ, recent literature has explored the use of this technique for bone tissue constructs aimed at large bone segmental defects [9,46–48].

The porosity of bone substitutes is crucial to allow for cell colonization and nutrient supply, and consequently, to permit bone remodeling. The role of pore geometry has been pointed out as a key to fostering cell proliferation and differentiation as well as tissue regeneration. Generally, interconnected porosity and pore sizes above 250 μm can trigger cell proliferation or differentiation [31,32]. In fact, several studies have pointed at the presence of concavities and sharp-edged pores as triggers for osteogenesis [49,50]. In our study, two types of geometries consisting of triangles, with acute angles and pore sizes of 200 μm , and hexagons averaging a size of 450 μm with higher number of obtuse angles were compared, including dense scaffolds as a control geometry without pores.

Moreover, mineral phases such as calcium phosphates improve the bioactivity and cell colonization when used as scaffolds or in combination with other substrates [51]. In our study, the presence of HA was evaluated biologically in two formats, direct exposure to the cells by surface HA coating (PLAcHA) or by indirect exposure to the HA embedded in the composite PLA15HA.

The presence of HA in both PLA15HA and PLAcHA samples was confirmed by ATR-FTIR. An increase on phosphate ν_4 bending modes at 560 and 600 cm^{-1} was observed in both samples, more obvious in composite PLA15HA due to the higher HA amount incorporated (Fig. 2b red arrows). Likewise, an increased intensity in the stretching mode for C-CH₃ in PLA at 1040 cm^{-1} overlapping the phosphate ν_3 bending at

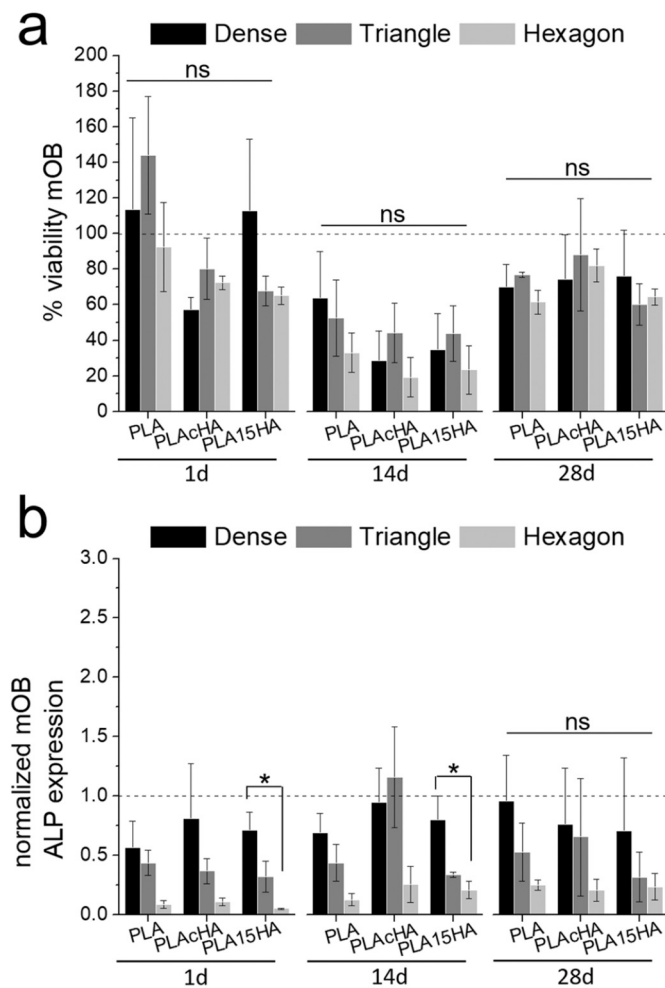


Fig. 8. Mouse osteoblasts (mOB) cell cultures on the different substrates and geometry; D, T, and H subscripts referring to dense, triangles, and hexagons, respectively, and substrates referred as PLA for pristine PLA, PLACHA for HA-coated PLA, and PLA15HA for the composite PLA with 15% wt. HA. (a) Cell proliferation over time measured by LDH and normalized to the area of the scaffolds and expressed as % compared to control samples (TCPS) at each time point (dotted line signifies 100% corresponding to controls); (b) ALP expression normalized to control samples (glass coverslips); * denotes statistical differences between the different geometries within the same substrate at each respective time point ($p < 0.05$), and ns stands for not significant ($p \geq 0.05$).

1030 cm^{-1} was observed in both substrates (Fig. 2b red arrows). Additionally, EDX analyses confirmed the presence of calcium and phosphorous (Fig. 4) on both substrates, with more intense signal for PLA15HA samples. The higher intensity of HA in composite PLA15HA samples was ascribed to the higher amount of HA incorporated quantified by TGA (Fig. 1b). The amount of HA in coated PLACHA was approximately 10-fold lower than in composite PLA15HA. The lack of signal from HA in the XRD measurements for the PLACHA samples could be attributed to the low amount of mineral, given the detection limit of the XRD [52].

Alkaline or acid treatment is often used to improve PLA hydrophilicity [53] or more engineered patterned surfaces using tight control of the etching procedure [54] by surface hydrolysis through the cleavage of the -C-O- ester bonds by hydroxides. In fact, the FTIR band corresponding to the ester group at 1747 cm^{-1} depicted a reduced intensity in etched PLACHA samples compared to neat PLA and composite PLA15HA samples as a result of the ester bonds cleavage. The microscopic images depicted a coverage of HA on the HA-coated PLACHA. Yaganida et al. demonstrated that the alkali treatment of PLA prior to HA coating

significantly improved the coverage of the PLA surface [37]. These particular coatings are comparable to biomimetic ones based in simulated body fluid, and similarly, they can render improved bioactivity, although the coating adhesion strength is usually below 10 MPa [55]. Our analyses of SEM images depicted smooth surfaces for PLA scaffolds, which was in accordance with the interferometry measurements (Fig. 5). An increase in surface roughness was observed for triangular and hexagonal pore geometries, inherent to their geometry structure. The highest increase in surface roughness was observed for composite PLA15HA (Fig. 5), in accordance with the SEM images, where visible particles embedded in the polymer matrix were observed. Despite the HA coverage of the surface in the coated PLACHA scaffolds, the HA coating did not significantly increase their overall roughness.

The thermal analyses by DSC further demonstrated the presence of HA in the composite PLA15HA (Fig. 1a). Higher crystallinity was found for composite PLA15HA samples, together with a reduction in the glass transition temperature (Fig. 1a, Table 1). This reduction in T_g is in accordance with previous literature ascribing a reduction of T_g when fillers such as HA or clay were incorporated into PLA [56,57]. A cold crystallization phenomenon was observed when HA was incorporated in the composite PLA15HA samples as reported by Senatov et al. in a study with similar composite filaments for 3D printing [57]. Interestingly, an enthalpy relaxation phenomenon was observed in all samples previously reported as polymer aging [58,59]. Similar to previous studies using PLA and talc for FDM printing, the relaxation enthalpy was reduced to half after the second heating endotherm (approx. 4–3 J/g for the first heating to 2–1 J/g) [58]. The effects of printing procedure and the geometry configuration on 3D printed PLA have been described by Baptista et al. [46]. They concluded that the printing process could affect the degree of crystallinity compared to pristine PLA, even without incorporation of fillers. The lowest crystallinity was shown for coated PLACHA, probably due to the alkali process used prior to HA coating. The thermal stability varied in PLA15HA similarly to reported by Ferri et al., with higher onset temperatures in degradation as the HA content increased [60].

Although the final goal incorporating mineral phases into polymers is to improve bioactivity, biocompatibility and the overall biological performance, the mechanical properties can also be enhanced. In such multiparametric approaches, the structural design, total porosity and pore size, and the composition of the scaffolds might impact the outcome both from a mechanical and biological perspective. Generally, the incorporation of minerals such as HA into polymers has shown to increase the elastic moduli and yield strength in FDM printed scaffolds. Grottkau et al. found 38% increase in the yield strength and 46% in the compressive modulus of 20% HA-PLA porous composites compared to PLA analogues [61]. Pitjmit et al. using non-porous scaffolds of PLA/PCL filled with 5 and 15% wt. HA reported enhanced compressive strength up to 83 MPa, compared to 77 MPa in absence of mineral fillers, although a decrease in the elastic moduli were reported [39]. On the other hand, pore sizes may affect the mechanical properties. Fairag et al. reported a decrease from 200 MPa to 150 MPa to 120 MPa as the pore sizes increased from 500 μm , to 750 μm , to 1000 μm , respectively in 3D printed PLA scaffolds [40]. Sahmani et al. reported an increase in compressive strength associated with the incorporation of HA combined with hexagonal pores [34].

A number of biocompatibility studies using 3D printed PLA-based scaffolds produced by FDM has emerged, although with some limitations, such as the use of immortalized cell lines, indirect biocompatibility assessment through extracts, and short periods of culture. In this work, both cell lines and primary cells were used on the 3D printed scaffolds, assessing viability, differentiation and mineralization over 28 days using osteogenic media. Experiments using Saos-2 cells showed cell viability lower than 70% in all scaffolds after 1 day, much more pronounced on PLACHA and PLA15HA samples than on pristine PLA samples. The possible presence of solvent traces in these samples, either from the ammonia etching process and the solvent mix with dichloromethane could be responsible for this phenomenon. However, all

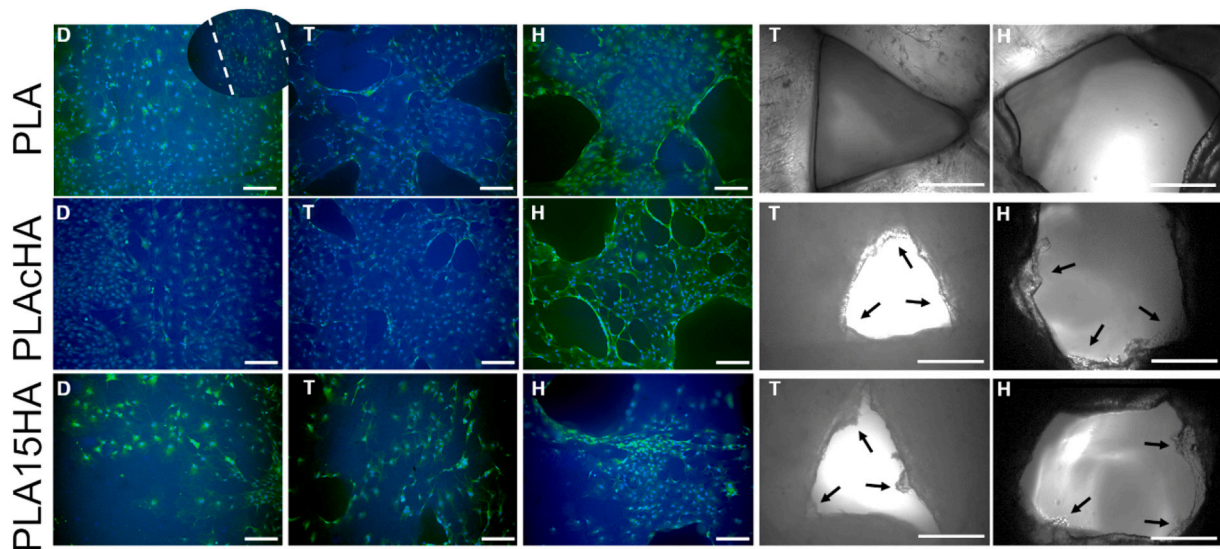


Fig. 9. Fluorescence and bright field images of the three substrates and geometries cultured with mOB after 28 days; D, T, and H correspond to dense, triangle and hexagon, respectively. First row and column insert shows a higher magnification image of dense PLA substrate cell alignment along the 3D printed threads (DAPI: blue, CFDA: green, scale bar: 200 μ m); bright field images for triangle and hexagon pore geometries illustrating matrix deposition at the pore edges and concavities (black arrows, scale bar: 200 μ m). (For interpretation of the references to colour in this figure legend, the reader is referred to the web version of this article.)

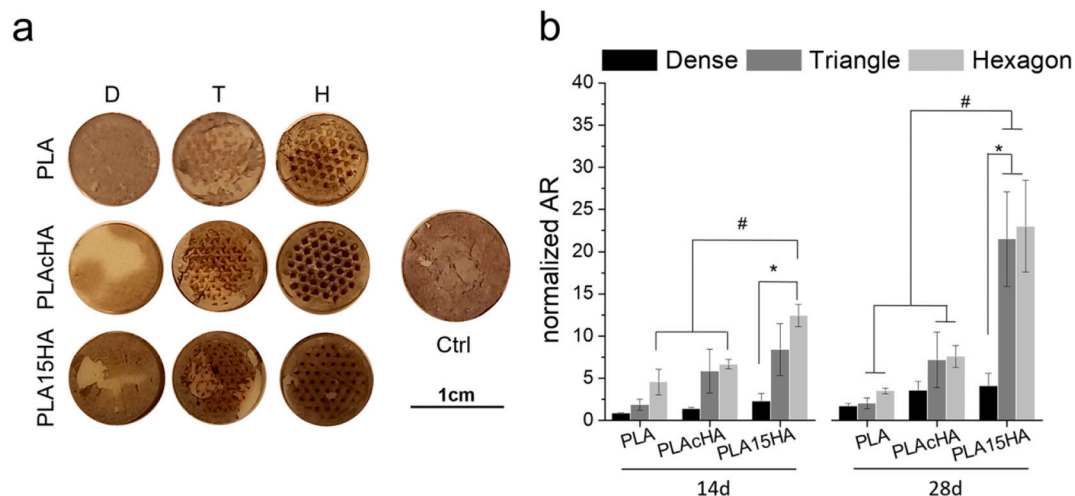


Fig. 10. Mineralization quantified by AR staining after 14 and 28 days using primary mouse osteoblasts. (a) AR stained scaffolds at 28 days (D, T, and H correspond to dense, triangle and hexagon). (b) AR quantification expressed normalized by control samples at 14 and 28 days; * denotes statistical differences between the different geometries within the same substrate at each respective time point, and # denotes statistical significance between the different type of substrates for each geometry ($p < 0.05$).

substrates and geometries supported cell proliferation after 14 and 28 days, reaching a viability that was higher than on control samples (tissue culture polystyrene). Few statistically significant differences were found when comparing geometries, although after 14 days porous scaffolds improved cell proliferation (Fig. 6a), and this trend was maintained after 28 days. Statistically significant differences were observed when comparing different substrate compositions, pointing at lower proliferative rates when HA was directly exposed to cells as compared to composite PLA15HA or pristine PLA.

Similar studies using mineral reinforced 3D printed polymers consisting of PLA and bioglass have also reported a lack of significant improvement by the mineral incorporation in cell viability [62]. Babilotte et al. reported a slightly increased adipocyte adhesion in the presence of 10% HA compared to pristine PLGA [26], although not statistically significant, similar to Orozco-Díaz et al. describing slight improvements in the presence of 20% HA [38]. In our study, no

improvement in cell viability was observed in the presence of HA, either present at surface level (PLAcHA) or embedded in the polymer matrix (PLA15HA; Fig. 8a). Likewise, cell differentiation as measured by ALP expression was not enhanced by the presence of HA in the scaffolds (Figs. 6b and 8b). Higher ALP activity of cells cultured on a composite of PLA and tricalcium phosphate (TCP) was reported by Zhang et al., although similar proliferative rates were described comparing 3D printed PLA-TCP composites, pristine TCP, or demineralized bone matrix [27]. Yang et al. observed an increase in ALP expression when using HA-coated PLA scaffolds via dopamine functionalization, although no improvement in cell viability was observed [63], and little improvement was achieved by silk fibroin coating when comparing PLA and composite PLA/HA [39].

The effects of pore sizes on osteoconduction and osteoinduction are controversial; studies using pristine PLA have demonstrated higher cell proliferation and differentiation when pores of 750 μ m were present

compared to 500 μm or 1000 μm [40], while others have shown no differences in cell proliferation with pore sizes varying between 150 and 250 μm [64]. In our experiments, synergistic effects of pore geometries and the presence of HA were noticeable in terms of increased mineralization and the ability of cells to populate scaffold crevices. Higher cell aggregation was observed on HA-containing scaffolds, and especially along pores. While pristine PLA scaffolds only showed certain cell alignment along printed threads, as reported by Grémare et al. [64], the presence of HA induced matrix deposition at the pore edges and concavities (Fig. 9), which is in accordance with previous works [40,62]. AR staining and quantification of mineralization in our study indicated enhanced mineralization in the presence of HA, consistent with previous studies [26,38,65]. In this work, the presence of hexagonal pores of approximately 450 μm together with the presence of HA enhanced mineralization to a greater extent than when 200 μm triangular pores were used (Fig. 10b). In fact, HA enhanced the presence of tissue deposition at pore concavities, which was not observed on pristine PLA scaffolds (Fig. 9, bright field images). Babilotte et al. found higher mineralization in the presence of 10% HA on PLGA porous scaffolds compared to pristine PLGA using human adipocytes [26]. Similarly, Orozco-Díaz et al. reported higher calcium and collagen deposition on 3D-printed PLA dense scaffolds by osteoblast cell line MG-63 when 5 and 20% HA were present compared to pure PLA, although 10% wt. HA incorporation had a negative effect on the elastic modulus of the samples [38].

While our study lacks an assessment of the reactions elicited in vivo, similar studies have shown PLA-based extruded materials to elicit mild inflammatory responses that, however, did not hamper heterotopic bone formation [19]. The levels of endotoxins in post-printed PLA-based porous scaffolds have been demonstrated to be below the food and drug administration (FDA) recommended levels [48].

5. Conclusions

The present study demonstrates the feasibility of producing customized filaments consisting of HA and PLA by cost-effective FDM printing with precise control of pore sizes and geometries. This allowed us to systematically vary the effects of both composition and pore geometry of experimental scaffolds on osteoconductivity. We observed only minor differences between scaffolds in terms of cell viability and osteoblastic differentiation up to four weeks. However, mineralization was strongly enhanced in the presence of both triangular and hexagonal pores, but only when HA was present, either as a coating or as a composite with PLA. These findings can guide the design of future scaffold designs for use in critical size bone defects, and they emphasize the importance of evaluating not only cellular adhesion, proliferation and differentiation, but to investigate mineralization since this process is a necessary requisite for actual osteoinductivity.

CRedit authorship contribution statement

A.D.E.: conceptualization, methodology, validation, investigation, formal analysis, visualization, writing-original draft, review, editing. **B.A.**: methodology, investigation, validation, writing-review & editing. **C.P.**: conceptualization, review-editing, funding acquisition. **N.P.H.**: conceptualization, methodology, writing-review & editing, supervision, project administration, funding acquisition.

Declaration of competing interest

The authors declare no conflict of interest.

Acknowledgements

The authors gratefully acknowledge the conceptual input in the design of synthetic materials intended for the repair of critical size bone

defects that was supplied by Anders Westermarck, MD. The authors would also like to thank Prof. Stefan Johansson for guidance during the printing process, and U-PRINT (Uppsala University's 3D-printing facility at the Disciplinary Domain of Medicine and Pharmacy) for access to filament extrusion facilities. ADE would like to thank Prof. Albert Mihrianyan for support performing thermal analyses, and Lars Hiertas Minne foundation (grant FO2018-0240). CP acknowledges Göran Gustafsson Foundation (grant number 1729) and Sweden's Innovation Agency VINNOVA through Competence Centre (2019-00029) for funding. NPH would like to thank the Swedish Research Council for funding (VR-2018-02612).

Appendix A. Supplementary data

Supplementary data to this article can be found online at <https://doi.org/10.1016/j.msec.2021.112091>.

References

- [1] H. Shegarfi, O. Reikeras, Review article: bone transplantation and immune response., *J. Orthop. Surg. (Hong Kong)*. 17 (2009) 206–211. doi:<https://doi.org/10.1177/230949900901700218>.
- [2] G.M. Calori, M. Colombo, E.L. Mazza, S. Mazzola, E. Malagoli, G.V. Mineo, Incidence of donor site morbidity following harvesting from iliac crest or RIA graft, *Injury*. 45 (2014) S116–S120, <https://doi.org/10.1016/j.injury.2014.10.034>.
- [3] E.H. Lee, J.C.H. Goh, R. Helm, R.W.H. Pho, Donor site morbidity following resection of the fibula, *J. Bone Jt. Surg. - Ser. B*. 72 (1990) 129–131, <https://doi.org/10.1302/0301-620x.72b1.2298771>.
- [4] L. Cvrček, F. Denk, Z. Čejka, Comparison of 3D printed trabecular structure with porous plasma spray: a method based on mapping the local modulus of elasticity, *Mater. Res. Express*. 7 (2020) 75403, <https://doi.org/10.1088/2053-1591/aba147>.
- [5] U. Homberg, D. Baum, S. Prohaska, J. Günster, S. Krauß-Schüler, Adapting trabecular structures for 3D printing: an image processing approach based on μ CT data, *Biomed. Phys. Eng. Express*. 3 (2017), 035027, <https://doi.org/10.1088/2057-1976/aa7611>.
- [6] D. Wu, A. Spanou, A. Díez-Escudero, C. Persson, 3D-printed PLA/HA composite structures as synthetic trabecular bone: a feasibility study using fused deposition modeling, *J. Mech. Behav. Biomed. Mater.* 103 (2020) 103608, <https://doi.org/10.1016/j.jmbbm.2019.103608>.
- [7] Y. Luo, Z. Lin, G. Guo, Biodegradation Assessment of Poly (Lactic Acid) Filled with Functionalized Titania Nanoparticles (PLA/TiO₂) under Compost Conditions, *Nanoscale Res. Lett.* 14 (2019) 56. doi:<https://doi.org/10.1186/s11671-019-2891-4>.
- [8] G. Dubinenko, A. Zinoviev, E. Bolbasov, A. Kozelskaya, E. Shesterikov, V. Novikov, S. Tverdokhlebov, Highly filled poly(L-lactic acid)/hydroxyapatite composite for 3D printing of personalized bone tissue engineering scaffolds, *J. Appl. Polym. Sci.* 138 (2021) 49662, <https://doi.org/10.1002/app.49662>.
- [9] N. Ranjan, R. Singh, I.P.S. Ahuja, R. Kumar, J. Singh, A.K. Verma, A. Leekha, On 3D printed scaffolds for orthopedic tissue engineering applications, *SN Appl. Sci.* 2 (2020). doi:<https://doi.org/10.1007/s42452-020-1936-8>.
- [10] M. Murariu, P. Dubois, PLA composites: from production to properties, *Adv. Drug Deliv. Rev.* 107 (2016) 17–46, <https://doi.org/10.1016/j.addr.2016.04.003>.
- [11] I. Manavitehrani, A. Fathi, H. Badr, S. Daly, A. Negahi Shirazi, F. Dehghani, Biomedical Applications of Biodegradable Polyesters, *Polymers (Basel)*. 8 (2016) 20. doi:<https://doi.org/10.3390/polym8010020>.
- [12] T. Kouya, S. Tada, H. Minbu, Y. Nakajima, M. Horimizu, T. Kawase, D.R. Lloyd, T. Tanaka, Microporous membranes of PLLA/PCL blends for periosteal tissue scaffold, *Mater. Lett.* 95 (2013) 103–106, <https://doi.org/10.1016/j.matlet.2012.12.076>.
- [13] H.-Y. Mi, M.R. Salick, X. Jing, B.R. Jacques, W.C. Crone, X.-F. Peng, L.-S. Turng, Characterization of thermoplastic polyurethane/poly(lactic acid) (TPU/PLA) tissue engineering scaffolds fabricated by microcellular injection molding, *Mater. Sci. Eng. C*. 33 (2013) 4767–4776, <https://doi.org/10.1016/j.msec.2013.07.037>.
- [14] T. Patrício, A. Glória, P. Bártolo, Mechanical and biological behaviour of PCL and PCL/PLA scaffolds for tissue engineering applications, in: *Chem. Eng. Trans., Italian Association of Chemical Engineering - AIChE*, 2013: pp. 1645–1650. doi:<https://doi.org/10.3303/CET1332275>.
- [15] T. Serra, M. Ortiz-Hernandez, E. Engel, J.A. Planell, M. Navarro, Relevance of PEG in PLA-based blends for tissue engineering 3D-printed scaffolds, *Mater. Sci. Eng. C*. 38 (2014) 55–62, <https://doi.org/10.1016/j.msec.2014.01.003>.
- [16] A. Barba, Y. Maazouz, A. Díez-Escudero, K. Rappe, M. Espanol, E.B. Montufar, C. Öhman-Mägi, C. Persson, P. Fontecha, M.-C. Manzaneres, J. Franch, M.-P. Ginebra, Osteogenesis by foamed and 3D-printed nanostructured calcium phosphate scaffolds: effect of pore architecture, *Acta Biomater.* 79 (2018) 135–147, <https://doi.org/10.1016/j.actbio.2018.09.003>.
- [17] A. Barba, A. Díez-Escudero, Y. Maazouz, K. Rappe, M. Espanol, E.B. Montufar, M. Bonany, J.M. Sadowska, J. Guillem-Marti, C. Öhman-Mägi, C. Persson, M.-C. Manzaneres, J. Franch, M.-P. Ginebra, Osteoinduction by foamed and 3D-printed calcium phosphate scaffolds: effect of nanostructure and pore architecture,

- ACS Appl. Mater. Interfaces 9 (2017) 41722–41736, <https://doi.org/10.1021/acsami.7b14175>.
- [18] S.V. Dorozhkin, Calcium orthophosphates in dentistry, *J. Mater. Sci. Mater. Med.* 24 (2013) 1335–1363, <https://doi.org/10.1007/s10856-013-4898-1>.
- [19] C.B. Danoux, D. Barbieri, H. Yuan, J.D. de Bruijn, C.A. van Blitterswijk, P. Habibovic, In vitro and in vivo bioactivity assessment of a polylactic acid/hydroxyapatite composite for bone regeneration, *Biomater.* 4 (2014), e27664, <https://doi.org/10.4161/biom.27664>.
- [20] H. Saniei, S. Mousavi, Surface modification of PLA 3D-printed implants by electrospinning with enhanced bioactivity and cell affinity, *Polymer (Guildf)* 196 (2020) 122467, doi:<https://doi.org/10.1016/j.polymer.2020.122467>.
- [21] C. Esposito Corcione, F. Gervaso, F. Scalera, F. Montagna, A. Sannino, A. Maffezzoli, The feasibility of printing polylactic acid-nanohydroxyapatite composites using a low-cost fused deposition modeling 3D printer, *J. Appl. Polym. Sci.* 134 (2017), doi:<https://doi.org/10.1002/app.44656>.
- [22] C. Esposito Corcione, F. Gervaso, F. Scalera, S.K. Padmanabhan, M. Madaghiele, F. Montagna, A. Sannino, A. Licciulli, A. Maffezzoli, Highly loaded hydroxyapatite microsphere/PLA porous scaffolds obtained by fused deposition modelling, *Ceram. Int.* 45 (2019) 2803–2810, <https://doi.org/10.1016/j.ceramint.2018.07.297>.
- [23] C. Esposito Corcione, F. Scalera, F. Gervaso, F. Montagna, A. Sannino, A. Maffezzoli, One-step solvent-free process for the fabrication of high loaded PLA/HA composite filament for 3D printing, *J. Therm. Anal. Calorim.* 134 (2018) 575–582, <https://doi.org/10.1007/s10973-018-7155-5>.
- [24] S.J. Kim, M.R. Kim, J.S. Oh, I. Han, S.W. Shin, Effects of polycaprolactone-tricalcium phosphate, recombinant human bone morphogenetic protein-2 and dog mesenchymal stem cells on bone formation: pilot study in dogs, *Yonsei Med. J.* 50 (2009) 825–831, <https://doi.org/10.3349/ymj.2009.50.6.825>.
- [25] R. De Santis, A. Gloria, T. Russo, U. D'Amora, S. Zeppetelli, A. Tampieri, T. Herrmannsdörfer, L. Ambrosio, A route toward the development of 3D magnetic scaffolds with tailored mechanical and morphological properties for hard tissue regeneration: preliminary study, *Virtual Phys. Prototyp.* 6 (2011) 189–195, <https://doi.org/10.1080/17452759.2011.631324>.
- [26] J. Babilotte, B. Martin, V. Guduric, R. Bareille, R. Agniel, S. Roques, V. Héroguez, M. Dussauze, M. Gaudon, D. Le Nihouannen, S. Catros, Development and characterization of a PLGA-HA composite material to fabricate 3D-printed scaffolds for bone tissue engineering, *Mater. Sci. Eng. C* 118 (2021) 111334, <https://doi.org/10.1016/j.msec.2020.111334>.
- [27] H. Zhang, X. Mao, Z. Du, W. Jiang, X. Han, D. Zhao, D. Han, Q. Li, Three dimensional printed macroporous polylactic acid/hydroxyapatite composite scaffolds for promoting bone formation in a critical-size rat calvarial defect model, *Sci. Technol. Adv. Mater.* 17 (2016) 136–148, <https://doi.org/10.1080/14686996.2016.1145532>.
- [28] H. Zhang, X. Mao, D. Zhao, W. Jiang, Z. Du, Q. Li, C. Jiang, D. Han, Three dimensional printed polylactic acid-hydroxyapatite composite scaffolds for prefabricating vascularized tissue engineered bone: an in vivo bioreactor model, *Sci. Rep.* 7 (2017) 1–13, <https://doi.org/10.1038/s41598-017-14923-7>.
- [29] S. Stener, L. Ejerhed, N. Sernert, G. Laxdal, L. Rostgård-Christensen, J. Kartus, A long-term, prospective, randomized study comparing biodegradable and metal interference screws in anterior cruciate ligament reconstruction surgery: radiographic results and clinical outcome, *Am. J. Sports Med.* 38 (2010) 1598–1605, <https://doi.org/10.1177/0363546510361952>.
- [30] P. Debieux, C.E.S. Franciozi, M. Lenza, M.J. Tamaoki, R.A. Magnussen, F. Faloppa, J.C. Bellotti, Bioabsorbable versus metallic interference screws for graft fixation in anterior cruciate ligament reconstruction, *Cochrane Database Syst. Rev.* 2016 (2016), <https://doi.org/10.1002/14651858.CD009772.pub2>.
- [31] V. Karageorgiou, D. Kaplan, Porosity of 3D biomaterial scaffolds and osteogenesis, *Biomaterials* 26 (2005) 5474–5491, <https://doi.org/10.1016/j.biomaterials.2005.02.002>.
- [32] R.A. Perez, G. Mestres, Role of pore size and morphology in musculo-skeletal tissue regeneration, *Mater. Sci. Eng. C* 61 (2016) 922–939, <https://doi.org/10.1016/j.msec.2015.12.087>.
- [33] A. Magnaudeix, J. Usseglio, M. Lasgorceix, F. Lalloue, C. Damia, J. Brie, P. Pascaud-Mathieu, E. Champion, Quantitative analysis of vascular colonisation and angio-conduction in porous silicon-substituted hydroxyapatite with various pore shapes in a chick chorioallantoic membrane (CAM) model, *Acta Biomater.* 38 (2016) 179–189, <https://doi.org/10.1016/j.actbio.2016.04.039>.
- [34] S. Sahmani, A. Khandan, S. Esmaeili, S. Saber-Samandari, M. Ghadiri Nejad, M. M. Aghdam, Calcium phosphate-PLA scaffolds fabricated by fused deposition modeling technique for bone tissue applications: fabrication, characterization and simulation, *Ceram. Int.* 46 (2020) 2447–2456, <https://doi.org/10.1016/j.ceramint.2019.09.238>.
- [35] E. Nyberg, A. Rindone, A. Dorafshar, W.L. Grayson, Comparison of 3D-printed poly-ε-caprolactone scaffolds functionalized with tricalcium phosphate, hydroxyapatite, bio-oss, or decellularized bone matrix, *Tissue Eng. Part A* 23 (2017) 503–514, <https://doi.org/10.1089/ten.tea.2016.0418>.
- [36] E. Nejati, V. Firouzdoz, M.B. Eslaminejad, F. Bagheri, Needle-like nano hydroxyapatite/poly(l-lactide acid) composite scaffold for bone tissue engineering application, *Mater. Sci. Eng. C* 29 (2009) 942–949, <https://doi.org/10.1016/j.msec.2008.07.038>.
- [37] H. Yanagida, M. Okada, M. Masuda, M. Ueki, I. Narama, S. Kitao, Y. Koyama, T. Furuzono, K. Takakuda, Cell adhesion and tissue response to hydroxyapatite nanocrystal-coated poly(l-lactide acid) fabric, *J. Biosci. Bioeng.* 108 (2009) 235–243, <https://doi.org/10.1016/j.jbiosc.2009.04.003>.
- [38] A. Orozco-Díaz, R. Moorehead, G.C. Reilly, F. Gilchrist, C. Miller, Characterization of a composite polylactic acid-hydroxyapatite 3D-printing filament for bone-regeneration, *Biomed. Phys. Eng. Express* 6 (2020) 25007, <https://doi.org/10.1088/2057-1976/ab73f8>.
- [39] S. Pitjamt, K. Thunsiri, W. Nakkiew, T. Wongwichai, P. Pothacharoen, W. Wattanuchariya, The possibility of interlocking nail fabrication from FFF 3D printing PLA/PCL/HA composites coated by local silk fibroin for canine bone fracture treatment, *Materials (Basel)* 13 (2020), doi:<https://doi.org/10.3390/ma13071564>.
- [40] R. Fairag, D.H. Rosenzweig, J.L. Ramirez-Garcialuna, M.H. Weber, L. Haglund, Three-dimensional printed polylactic acid scaffolds promote bone-like matrix deposition in vitro, *ACS Appl. Mater. Interfaces* 11 (2019) 15306–15315, <https://doi.org/10.1021/acsami.9b02502>.
- [41] J.R. Sarasua, A.L. Arraiza, P. Balerdi, I. Maiza, Crystallinity and mechanical properties of optically pure polylactides and their blends, *Polym. Eng. Sci.* 45 (2005) 745–753, <https://doi.org/10.1002/pen.20331>.
- [42] M. Cámara-Torres, R. Sinha, C. Mota, L. Moroni, Improving cell distribution on 3D additive manufactured scaffolds through engineered seeding media density and viscosity, *Acta Biomater.* 101 (2020) 183–195, <https://doi.org/10.1016/j.actbio.2019.11.020>.
- [43] M. Puchalski, S. Kwolek, G. Szparaga, M. Chrzanowski, I. Krucinska, Investigation of the influence of PLA molecular structure on the crystalline forms (α' and α) and Mechanical Properties of Wet Spinning Fibres, *Polymers (Basel)* 9 (2017), doi:<https://doi.org/10.3390/polym9010018>.
- [44] H.N. Chia, B.M. Wu, Recent advances in 3D printing of biomaterials, *J. Biol. Eng.* 9 (2015), doi:<https://doi.org/10.1186/s13036-015-0001-4>.
- [45] S. Bose, S. Vahabzadeh, A. Bandyopadhyay, Bone tissue engineering using 3D printing, *Mater. Today* 16 (2013) 496–504, <https://doi.org/10.1016/j.MATOD.2013.11.017>.
- [46] R. Baptista, M. Guedes, Morphological and mechanical characterization of 3D printed PLA scaffolds with controlled porosity for trabecular bone tissue replacement, *Mater. Sci. Eng. C* 118 (2021) 111528, <https://doi.org/10.1016/j.msec.2020.111528>.
- [47] C.A. Dascalu, F. Miculescu, A.C. Mocanu, A.E. Constantinescu, T.M. Butte, A.M. Pandele, R.C. Ciocoiu, S.I. Voicu, L.T. Ciocan, Novel synthesis of core-shell biomaterials from polymeric filaments with a bioceramic coating for biomedical applications, *Coatings* 10 (2020), doi:<https://doi.org/10.3390/coatings10030283>.
- [48] U. Ritz, R. Gerke, H. Götz, S. Stein, P.M. Rommens, A new bone substitute developed from 3D-prints of polylactide (PLA) loaded with collagen I: An in vitro study, *Int. J. Mol. Sci.* 18 (2017), doi:<https://doi.org/10.3390/ijms18122569>.
- [49] P.Y. Huri, B. Arda Ozilgen, D.L. Hutton, W.L. Grayson, Scaffold pore size modulates in vitro osteogenesis of human adipose-derived stem/stromal cells, *Biomed. Mater.* 9 (2014), 045003, <https://doi.org/10.1088/1748-6041/9/4/045003>.
- [50] Z. Chen, X. Yan, S. Yin, L. Liu, X. Liu, G. Zhao, W. Ma, W. Qi, Z. Ren, H. Liao, M. Liu, D. Cai, H. Fang, Influence of the pore size and porosity of selective laser melted Ti6Al4V ELI porous scaffold on cell proliferation, osteogenesis and bone ingrowth, *Mater. Sci. Eng. C* 106 (2020), doi:<https://doi.org/10.1016/j.msec.2019.110289>.
- [51] J. Jeong, J.H. Kim, J.H. Shim, N.S. Hwang, C.Y. Heo, Bioactive calcium phosphate materials and applications in bone regeneration, *Biomater. Res.* 23 (2019) 1–11, <https://doi.org/10.1186/s40824-018-0149-3>.
- [52] K.L. Vyverberg, J.M. Jaeger, A. Dutton, Quantifying detection limits and uncertainty in X-ray diffraction mineralogical assessments of biogenic carbonates, *J. Sediment. Res.* 88 (2018) 1261–1275, <https://doi.org/10.2110/jsr.2018.63>.
- [53] L.F. Charles, M.T. Shaw, J.R. Olson, M. Wei, Fabrication and mechanical properties of PLLA/PCL/HA composites via a biomimetic, dip coating, and hot compression procedure, *J. Mater. Sci. Mater. Med.* 21 (2010) 1845–1854, <https://doi.org/10.1007/s10856-010-4051-3>.
- [54] C. Cummins, P. Mokarian-Tabari, J.D. Holmes, M.A. Morris, Selective etching of polylactic acid in poly(styrene)-block-poly(d,l) lactide diblock copolymer for nanoscale patterning, *J. Appl. Polym. Sci.* 131 (2014) 9493–9504, doi:<https://doi.org/10.1002/app.40798>.
- [55] H. Qu, M. Wei, Improvement of bonding strength between biomimetic apatite coating and substrate, *J. Biomed. Mater. Res. - Part B Appl. Biomater.* 84 (2008) 436–443, <https://doi.org/10.1002/jbm.b.30889>.
- [56] M. Pluta, M.-A. Paul, M. Alexandre, P. Dubois, Plasticized polylactide/clay nanocomposites. I. The role of filler content and its surface organo-modification on the physico-chemical properties, *J. Polym. Sci. Part B Polym. Phys.* 44 (2006) 299–311, doi:<https://doi.org/10.1002/polb.20694>.
- [57] F.S.F. Senatov, K.V.K. Niaza, My.Y. Zadorozhnyy, A.V.A. Maksimkin, S.D. Kaloshkin, Y.Z.Y. Estrin, Mechanical properties and shape memory effect of 3D-printed PLA-based porous scaffolds, *J. Mech. Behav. Biomed. Mater.* 57 (2015) 139–148, doi:<https://doi.org/10.1016/j.jmbbm.2015.11.036>.
- [58] W. Yu, X. Wang, E. Ferraris, J. Zhang, Melt crystallization of PLA/talc in fused filament fabrication, *Mater. Des.* 182 (2019) 108013, <https://doi.org/10.1016/j.matdes.2019.108013>.
- [59] I.M. Hodge, A.R. Berens, Effects of Annealing and Prior History on Enthalpy Relaxation in Glassy Polymers. 2. Mathematical Modeling, *Macromolecules* 15 (1982) 762–770, doi:<https://doi.org/10.1021/ma00231a016>.
- [60] J.M. Ferri, D.L. Motoc, S.F. Bou, R. Balart, Thermal expansivity and degradation properties of PLA/HA and PLA/βTCP in vitro conditioned composites, *J. Therm. Anal. Calorim.* 138 (2019) 2691–2702, <https://doi.org/10.1007/s10973-019-08799-0>.
- [61] B.E. Grottkau, Z. Hui, Y. Yao, Y. Pang, Rapid fabrication of anatomically-shaped bone scaffolds using indirect 3D printing and perfusion techniques, *Int. J. Mol. Sci.* 21 (2020), doi:<https://doi.org/10.3390/ijms21010315>.
- [62] T. Distler, N. Fournier, A. Grünwald, C. Polley, H. Seitz, R. Detsch, A.R. Boccaccini, Polymer-Bioactive Glass Composite Filaments for 3D Scaffold Manufacturing by Fused Deposition Modeling: Fabrication and Characterization,

- Front. Bioeng. Biotechnol. 8 (2020). doi:<https://doi.org/10.3389/fbioe.2020.00552>.
- [63] W.F. Yang, L. Long, R. Wang, D. Chen, S. Duan, F.J. Xu, Surface-modified hydroxyapatite nanoparticle-reinforced polylactides for three-dimensional printed bone tissue engineering scaffolds, *J. Biomed. Nanotechnol.* 14 (2018) 295–303, <https://doi.org/10.1166/jbn.2018.2495>.
- [64] A. Grémare, V. Guduric, R. Bareille, V. Heroguez, S. Latour, N. L'heureux, J.-C. Fricain, S. Catros, D. Le Nihouannen, Characterization of printed PLA scaffolds for bone tissue engineering, *J. Biomed. Mater. Res. Part A*. 106 (2018) 887–894, <https://doi.org/10.1002/jbm.a.36289>.
- [65] M. Persson, P.P. Lehenkari, L. Berglin, S. Turunen, M.A.J. Finnilä, J. Risteli, M. Skrifvars, J. Tuukkanen, Osteogenic differentiation of human mesenchymal stem cells in a 3D woven scaffold, *Sci. Rep.* 8 (2018) 1–12, <https://doi.org/10.1038/s41598-018-28699-x>.